Journal of Hazardous Materials 499 (2025) 140171

Contents lists available at ScienceDirect

Journal of Hazardous Materials

journal homepage: www.elsevier.com/locate/jhazmat

Efficient removal of polystyrene nanoplastics from complex water system through multiple driving forces with MOF-based composite

Shiqian Zhou [a,b], Xiao Wang [a], Xujing Chen [a,b], Shijie Yang [a,b], Kai Chen [a], Guanqing Song [a,b], Guanhong Lu [a], Yan Wang [a], Jing Sun [a,*]

[a] State Key Lab of High Performance Ceramics and Superfine Microstructure, Shanghai Institute of Ceramics, Chinese Academy of Sciences, 585 Heshuo Road, Shanghai 201899, China
[b] University of Chinese Academy of Sciences, 19 (A) Yuquan Road, Beijing 100049, China

HIGHLIGHTS

- MOF-based composite was fabricated via an in-situ synthesis strategy.
- Synergistic multiple driving forces boost nanoplastics capture efficiency.
- The influence of real aqueous environment on adsorption was deeply investigated.
- The foam exhibits excellent reusability, recyclability and acid-base resistance.

GRAPHICAL ABSTRACT

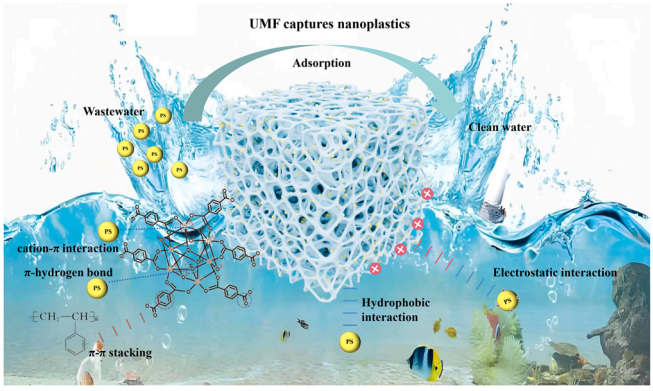

ARTICLE INFO

Keywords:
Nanoplastics
UIO-66
MOF-based composite
Adsorption
Multiple driving forces

ABSTRACT

As emerging contaminants widely present in aquatic environments, micro/nano plastics (MPs/NPs) pose global environmental and biosafety concerns. The efficient removal of MPs/NPs faces challenges such as poor selectivity and low cyclic stability of traditional adsorbents. This study developed an in-situ synthesis strategy to integrate UIO-66 with melamine foam (MF), successfully constructing UIO-66/MF (UMF) composite that combined high adsorption capacity with excellent structural stability. The results showed that UMF achieved adsorption equilibrium for PS NPs within 300 min, with an adsorption capacity of 65.5 mg/g. Moreover, UMF maintained over 93 % and 82 % adsorption efficiency in a broad pH range (3−10) and under complex aqueous conditions, respectively. Mechanistic analysis revealed that multiple synergistic interactions were involved in the adsorption process, including hydrophobic interactions, electrostatic interactions, π-π stacking, hydrogen bonding and cation-π interactions. Furthermore, we systematically disclosed the factors which led to the decreased adsorption efficiency in tap water and river water. Notably, UMF exhibited exceptional reusability, retaining higher than 81 % removal efficiency after 25 cycles. UMF effectively addresses the challenges of MOFs powders instability

* Corresponding author.
E-mail address: jingsun@mail.sic.ac.cn (J. Sun).

https://doi.org/10.1016/j.jhazmat.2025.140171
Received 3 July 2025; Received in revised form 29 September 2025; Accepted 16 October 2025
Available online 17 October 2025

and recycling difficulties, achieving a balance between economy, sustainability, and practicality. This composite provides a promising solution for remediating MPs/NPs pollution in aqueous environments.

1. Introduction

Microplastics (MPs) and nanoplastics (NPs), as global emerging pollutants, have become a focal point in environmental science for their environmental and ecological risk [1]. Currently, researchers classify plastic fragments smaller than 5 mm as MPs [2], while NPs are usually considered to be plastic particles smaller than 1 μm [3]. NPs often pose a more serious risk to the cells of living organisms than MPs due to their higher reactivity and bioavailability [4]. Research has confirmed that global annual plastic production has exceeded 320 million tons, yet approximately 8 million tons of plastic waste ultimately flow into the oceans each year due to the durability and persistence of plastic materials [5]. MPs and NPs exhibit degradation resistance, and their high specific surface area enables them to accumulate various toxic contaminants in aquatic environments, including pharmaceutical residues, heavy metal ions, and persistent organic pollutants [6]. The small size of MPs and NPs makes them easily ingestible by aquatic organisms, allowing them to enter the human food chain. Evidence has shown that MPs were found in human feces, body fluids, and organs, including blood, urine, and even the placenta [7–10]. In recent years, studies have further revealed that MPs and NPs could penetrate cell membranes, inducing oxidative stress and inflammatory responses, and even disrupting endocrine system functions [11–14], posing a serious threat to human health. Considering the increasing severity of MPs pollution and its detrimental impacts, the effective remediation of MPs and NPs from water has become an urgent necessity for clean water access and sustainable future development.

Currently, the primary methods for MPs removal include filtration, flocculation, and adsorption. Membrane filtration is prone to membrane fouling and clogging, resulting in high operational costs [15]. The use of chemical reagents in water treatment makes flocculation less environmentally friendly, and its removal efficiency for MPs smaller than 125 μm is particularly poor [16]. In recent years, the adsorption method has been regarded as a potential solution for the deep removal of MPs due to its operational flexibility and low energy consumption [17]. Although traditional adsorption materials (such as activated carbon and biochar) possess certain adsorption capabilities, their applications are limited by issues including restricted specific surface area, poor selectivity, and difficulties in regeneration [18,19]. Therefore, researchers have also developed several new adsorbent materials. For instance, the starch-gelatin sponge fabricated by Chen et al. exhibited effective adsorption of MPs [20]. However, its performance was susceptible to pH variations and showed a significant decline in efficiency when applied to real water samples. Another example, chitin and graphene oxide sponges, demonstrated good mechanical strength, but their adsorption capacity for PS was only 5.898 mg/g, coupled with poor recyclability [21]. The above adsorbents still failed to meet the requirements for efficient and sustainable removal of MPs/NPs.

Metal-Organic Frameworks (MOFs) show significant potential in the field of pollutant adsorption by virtue of their ultra-high specific surface area, tunable pore structure and surface functionalization [22–25]. Research has confirmed that MOFs can effectively capture MPs/NPs. ZIF-67 achieved a 92.1 % adsorption efficiency for PS MPs through primary electrostatic interactions and partial π-π stacking interactions [26]. Similarly, MIL-101(Cr) removed 96 % of negatively charged 65 nm PS NPs at pH 5 due to its positively charged surface [27]. However, current research still faces significant limitations. Firstly, most MOFs used in powder form are prone to loss with water flow, suffer from aggregation and difficult to be recovered, and experience severe efficiency degradation after multiple cycles, thus limiting their practical applications [28]. Secondly, research on the adsorption mechanism of MPs focuses on a single force (e.g., electrostatic interaction), and lacks a systematic analysis of the synergistic effect of multiple mechanisms such as hydrogen bonding and hydrophobic interaction. Moreover, the impact of high ionic strength and complex organic coexistence in actual water bodies on adsorption performance remains unclear. Therefore, developing MOF-based composite materials with high stability, environmental adaptability and easy recovery characteristics has become a crucial breakthrough for advancing MPs/NPs treatment technologies.

Herein, to address the aforementioned challenges, this study proposed the construction of UMF composite through an in-situ growth strategy using MF as a multifunctional carrier, aiming to achieve efficient removal and resource recovery of MPs/NPs. The three-dimensional interconnected channels of MF provided favorable spaces for MOF growth, preventing nanoparticles aggregation while ensuring rapid solvent penetration. The adsorption kinetics, environmental influencing factors, adsorption mechanisms and regeneration performance of UMF for PS NPs were systematically investigated. Additionally, this approach resolved the issues of difficult separation and recovery of MOF powders. The mechanical stability of MF combined with the hydrothermal stability of UIO-66 ensures long-term reusability in complex water environments. This material enables the efficient removal of NPs, offering a sustainable and practical technological pathway for complex water pollution treatment.

2. Materials and methods

2.1. Chemicals

Zirconium chloride ($ZrCl_4$, 98 %), terephthalic acid (H_2BDC, $C_8H_6O_4$, 99 %), N,N-Dimethylformamide (DMF, C_3H_7NO, 99.5 %), acetic acid (CH_3COOH), calcium chloride ($CaCl_2$), magnesium chloride ($MgCl_2$), and iron chloride ($FeCl_3$) were purchased from Adamas Corporation (Shanghai, China). Sodium chloride (NaCl) and sodium sulfate (Na_2SO_4) were obtained from Shanghai General Reagent Technology Co., Ltd. Sodium carbonate (Na_2CO_3) and sodium phosphate (Na_3PO_3) were purchased from China Sinopharm Chemical Reagent Co., Ltd. Anhydrous ethanol (EtOH, C_2H_5OH) was provided by Shanghai Lingfeng Chemical Reagent Co., Ltd. Deionized water (DI, H_2O) was supplied by a Milli-Q system produced by Shanghai Tongji Scientific Instrument Co., Ltd. MF was purchased from Taobao, and PS (500 nm) NPs were obtained from Jiangsu Zhichuan Technology Co., Ltd. All chemical reagents used in the experiments were of analytical grade and used without further purification.

2.2. Preparation of UMF

Firstly, the pristine MF was ultrasonically cleaned in a 3 mol/L CH_3COOH solution for 6 h, followed by drying and storage. Subsequently, 1 mmol of $ZrCl_4$, H_2BDC, and cleaned MF were weighed and added to 30 mL of DMF solution, followed by thorough ultrasonic dissolution. The solution along with MF was then transferred into an autoclave and reacted at 120 °C for 24 h. After the autoclave was cooled down, the obtained material was washed three times with DMF and EtOH, respectively, and vacuum-dried at 80 °C for 12 h. The synthesis of UIO-66 followed identical procedures without MF addition. MF used in the synthesis process weighed 14.3 mg and its size was 2 × 1 × 1 cm.

2.3. Characterization

The crystal structure of the samples was obtained using an X-ray diffractometer (XRD, D8 ADVANCE) equipped with Cu Kα radiation,

with a scanning angle range of 5° to 60° and a scanning speed of 5°/min. The surface morphology of the samples was observed using a scanning electron microscope (SEM, FEI Magellan 400). Fourier transform infrared spectroscopy (FTIR) was measured on Thermo Fisher Scientific Nicolet iS20 (USA). The water contact angle was tested using a dynamic contact angle instrument (Kunshan Shengding SDC 350KS). The specific surface area and pore structure of the samples were measured using a surface area and porosity analyzer (Jingwei Gaobo). The zeta potential of PS and UIO-66 at different pH levels (adjusted to the desired pH using 0.1 M HCl and NaOH) was tested with zetasizer (zetaPlus, Brookhaven). X-ray photoelectron spectroscopy (XPS) was performed using a Thermo Scientific K-Alpha (USA) instrument to analyze elemental valence states and surface chemical environments. The UV-Vis absorption spectra of PS were recorded using a UV-Vis spectrophotometer (PerkinElmer Lambda 1050 +, USA), with deionized water as the background standard. The concentrations of metal ions in tap water and river water were detected using an inductively coupled plasma optical emission spectrometer (ICP-OES/MS, Thermo Fisher iCAP PRO, USA). The anion concentrations in tap water and river water were analyzed using an ion chromatograph (IC, Thermo Scientific ICS 2100, USA).

2.4. Adsorption experiment

PS has been selected as model pollutant because of its extensive use in products like disposable tableware, packaging, and appliance casings, which makes it one of the most ubiquitous MPs in aquatic environments [29]. UMF was added to reagent bottles containing 10 mL of PS solution (100 mg/L), followed by being shaken in a constant temperature oscillator at 220 r/min at room temperature. The UV-Vis absorption spectra of PS solutions were measured from 250 to 800 nm using deionized water as the blank reference. The maximum absorption peak of PS solution was observed at 276 nm (Fig. S1a). A concentration-absorbance standard curve was established by measuring the absorbance at 276 nm for PS solutions with different concentrations (Fig. S1b). The concentration of residual PS in the solution after adsorption was calculated based on the established standard curve. For the adsorption kinetics study, the residual PS concentrations in the solution were recorded at different shaking times (10, 30, 60, 120, 180, 300, 420, 540 and 720 min), and the removal efficiency at each time point was calculated accordingly. The adsorption isotherm was measured and analyzed by setting the initial PS concentrations at 25, 50, 100, 200, 225, and 250 mg/L at 25 °C. To investigate the effect of pH on PS adsorption by UMF, the pH of the PS solution was adjusted to the desired values (3−10) using 0.1 M HCl or NaOH while keeping other factors unchanged. Additionally, the influence of ionic strength on PS removal was examined by adding Cl^-、NO_3^-、SO_4^{2-}、CO_3^{2-}、PO_4^{3-}、Na^+、Ca^{2+}、Mg^{2+} and Fe^{3+}. Finally, to validate the practical application performance of the material, adsorption experiments were conducted using tap water from the Shanghai Institute of Ceramics, river water from Pingcheng Road River, Shanghai, and sea water from Huludao. Unless otherwise specified, all experiments were performed at pH 6 and 25 °C, with triplicate parallel adsorption tests conducted simultaneously. The removal efficiency (R_e, %) and adsorption capacity (q_e, mg/g) of UMF were calculated using Eqs. (1) and (2):

$$R_e = \frac{C_0 - C_t}{C_0} \times 100\% \quad (1)$$

$$q_e = (C_0 - C_t) \times \frac{V}{m} \quad (2)$$

where C_0 (mg/L) represents the initial concentration of PS, C_t (mg/L) represents the concentration of PS at different reaction times, V (L) represents the volume of PS solution, and m (g) is the mass of UMF adsorbent.

2.5. Reusability of UMF adsorbents

In order to study the reproducibility of UMF adsorbent, the PS absorbed by UMF was desorbed by DMF and ethanol. Briefly, the adsorbed UMF was washed by immersing it into DMF solution with oscillation, and then, rinsed twice with anhydrous ethanol. Finally, the UMF was dried for the next adsorption cycle. Recoverability was assessed by repeating the adsorption process for 25 cycles with PS concentration as 50 mg/L.

2.6. Statistical Analysis

All experiments were performed in triplicate, and the results were presented as mean values. Error bars in the figures represent standard deviation (n = 3).

3. Results and discussion

3.1. Characterization of UMF

Fig. 1 illustrates the preparation route of UMF. A certain amount of metal source and ligand were dissolved in DMF, followed by placing the pretreated MF into the solution. After thorough ultrasonic dissolution, the mixture was transferred to an autoclave, where UIO-66 self-assembled onto the melamine foam through a solvothermal process. Fig. 2 displays the microscopic morphologies of pristine MF and UMF. The pristine MF exhibited a smooth three-dimensional interconnected network structure with pore sizes of approximately 100 μm (Fig. 2a-c). Compared to the pristine foam, the UMF skeleton surface changed from smooth to rough, with UIO-66 nanoparticles uniformly covered on the foam framework (Fig. 2d-f). Further magnification revealed that UIO-66 had a hexahedral structure (particle size ~200 nm) (Fig. S2), consistent with the results reported by other researchers [30]. The foam maintained the hierarchical pore structure after the growth of UIO-66 nanoparticles. Energy-dispersive spectroscopy (EDS) analysis of the elemental composition in UMF showed the presence of C, N, O and Zr (Fig. 2g), with Zr originating from UIO-66 and uniformly distributed. Both SEM and EDS results proved the successful growth of UIO-66 on the MF framework.

XRD analysis (Fig. 3a) revealed that the pristine MF exhibited an amorphous structure, while UMF showed strong diffraction peaks characteristic of UIO-66, indicating the formation of UIO-66 within the MF framework. Furthermore, FTIR spectra (Fig. 3b) confirmed the integration of UIO-66 with MF. The peaks of UMF at 1545, 1321, and 809 cm^{-1} were attributed to the C═N stretching of the triazine ring, C-N stretching of the s-triazine ring, and bending vibration of the triazine ring in pristine MF, respectively [31]. Simultaneously, the peaks at 1579 and 1504 cm^{-1} in UMF corresponded to the C═C stretching vibrations of the benzene ring in H_2BDC molecules [32,33], while the peaks at 1654 and 1394 cm^{-1} represented the asymmetric and symmetric stretching vibrations of -COO groups, respectively [34]. The peaks at 744 and 664 cm^{-1} were associated with the symmetric and asymmetric vibrations of O-Zr-O bonds [35], further confirming the formation of $Zr_6(OH)_4O_4$ clusters [36]. The appearance of these characteristic vibration peaks indicated the formation of distinctive chemical bonds in UIO-66. The comprehensive analysis from multiple techniques sufficiently denoted the successful loading of UIO-66 on the MF substrate and the structural integrity of the composite.

Nitrogen adsorption-desorption isotherm showed the variations in specific surface area (Fig. 3c) and pore characteristics (Fig. 3d) of the material (Table 1). The pristine MF exhibited a specific surface area of merely 10.80 m^2/g, with pore characteristics typical of mesoporous materials. After UIO-66 loading, UMF demonstrated a significant increase in specific surface area to 45.73 m^2/g, representing a 4.5-fold enhancement, while maintaining the mesoporous-dominated pore structure. UIO-66 displayed typical Type I isotherm characteristics of

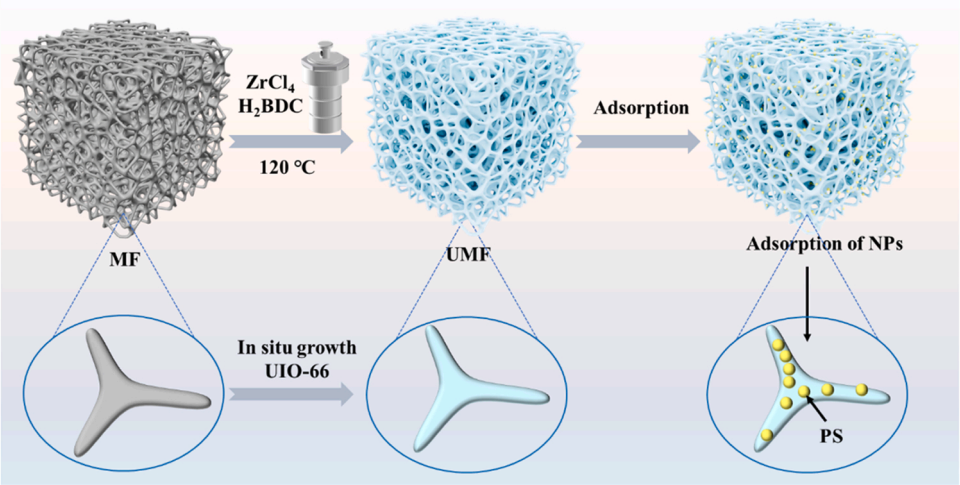

Fig. 1. Schematic diagram of UMF synthesis and PS removal.

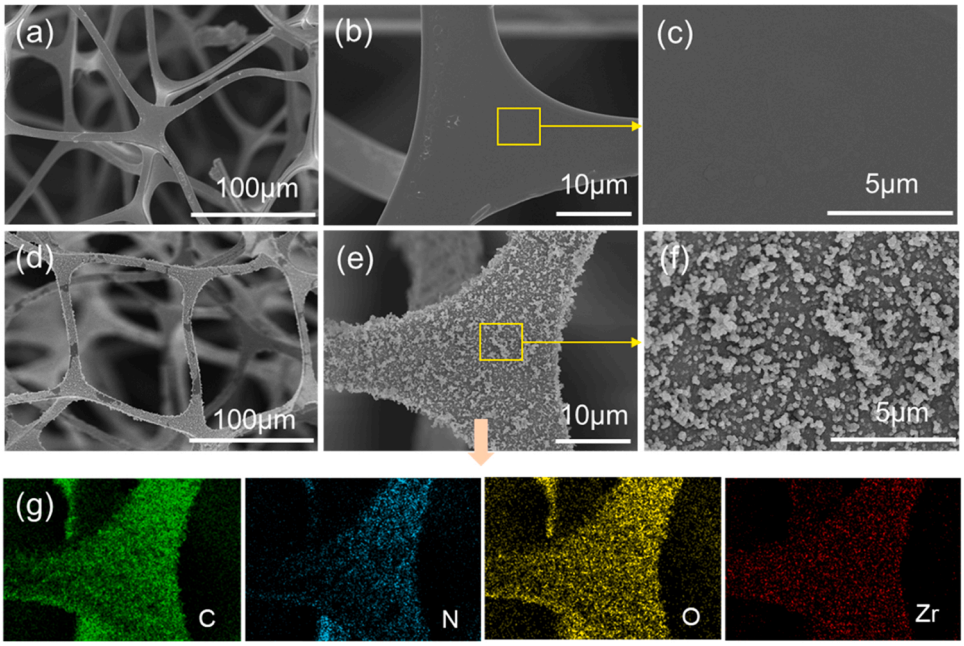

Fig. 2. SEM of the MF (a), (b) and (c) and UMF (d), (e) and (f), (g) Mapping element spectra of the UMF.

microporous materials, with a remarkably high specific surface area of 805.29 m^2/g. The pore size distribution curve (Fig. S3) confirmed that this material primarily consisted of micropores smaller than 2 nm. The increased surface area of UMF compared to pristine MF implies the exposure of more active sites, thereby enhancing adsorption efficiency.

Hydrophobic interactions play a crucial role in the adsorption process of MPs/NPs by materials [37]. As shown in Fig. S4, MF exhibited a water contact angle of 4.5° indicating its superhydrophilicity, while UMF showed a water contact angle of 134°, indicating a hydrophobic surface. Notably, the hydrophobicity of UMF originates from the uniformly loaded UIO-66 on its surface. Since most MPs/NPs particles exhibited hydrophobic surfaces, UMF could preferentially capture MPs/NPs particles through hydrophobic-hydrophobic interactions, thereby effectively reducing competitive adsorption from coexisting substances in water and significantly enhancing the selectivity and efficiency of MPs removal [38]. In our experiments, MF showed almost no adsorption capability for PS (Fig. S5a), while UMF showed exceptionally strong adsorption of MPs (Fig. S5b), further confirming that hydrophobic interactions promote MPs adsorption.

3.2. Adsorption kinetics

Initially, we investigated the effect of adsorption time on the adsorption capacity of UMF. Fig. 4a displayed that the adsorption efficiency of PS NPs with concentration of 50 mg/L increased to 63.0 % within 10 min and gradually reached 100 % within 60 min. High-concentration (100 mg/L) PS NPs achieved a high removal efficiency of 58.6 % within 30 min and gradually approached 100 % removal efficiency within 300 min. These results revealed the rapid kinetic adsorption process of PS. The equilibrium adsorption capacities for 50 mg/L and 100 mg/L PS suspensions were 32.9 mg/g and 65.5 mg/g, respectively (Fig. 4b).

To better explain the entire adsorption process, we applied pseudo-first-order, pseudo-second-order and intra-particle diffusion models for linear fitting of PS at different concentrations. The three kinetic fitting equations are presented as follows.

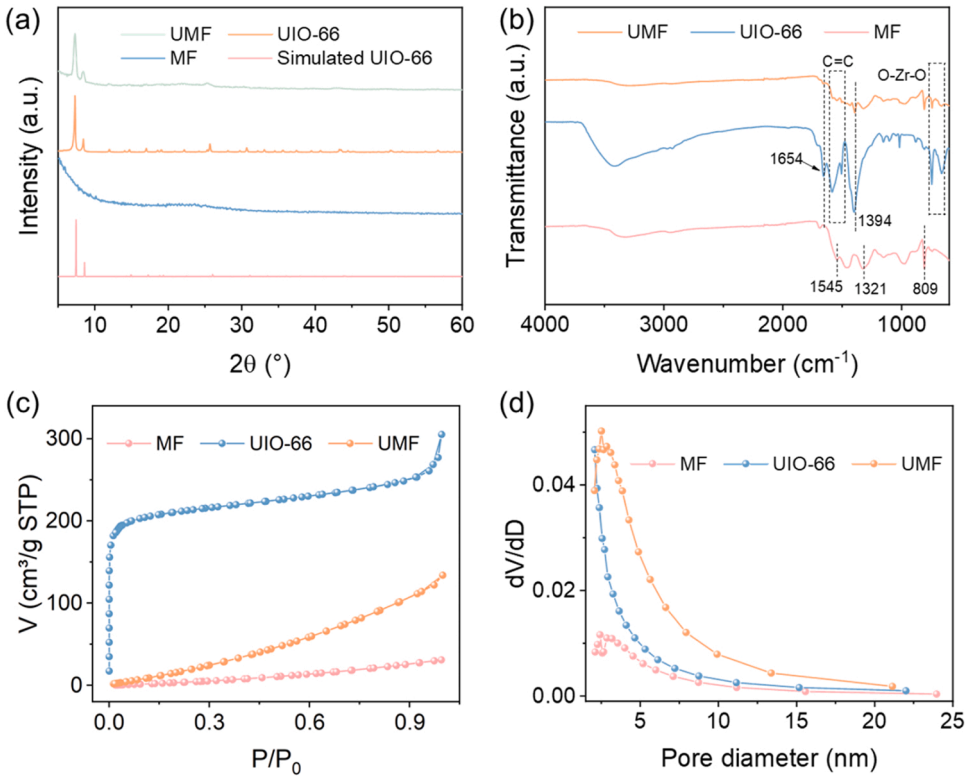

Fig. 3. (a) XRD patterns, (b) FTIR spectra, (c) N_2 adsorption-desorption isotherms and (d) the pore size distributions of MF, UIO-66 and UMF.

Table 1
Specific surface area of different samples.

Samples	S_{BET} (m^2/g)	V_t (cm^3/g)
MF	10.80	0.039
UMF	45.73	0.150
UIO−66	805.29	0.446

$$\ln(q_e - q_t) = \ln q_e - k_1 t \tag{3}$$

$$\frac{t}{q_t} = \frac{1}{k_2 q_e^2} + \frac{t}{q_e} \tag{4}$$

$$q_t = k_p t^{0.5} + C \tag{5}$$

where q_e (mg/g) and q_t (mg/g) represent the adsorption capacities of UMF at equilibrium and at time t (h), respectively. k_1 (min^{-1}) is the rate constant of the pseudo-first-order reaction, and k_2 ($g{\cdot}mg^{-1}{\cdot}min^{-1}$) is the rate constant of the pseudo-second-order reaction. k_p ($mg{\cdot}g^{-1}{\cdot}min^{-0.5}$) denotes the intra-particle diffusion rate constant. C (mg/g) is a constant related to the thickness of the boundary layer.

The kinetic fitting results and relevant parameters of UMF for PS are presented in Fig. 4c and d, and Tables S1-S3. The findings showed that the pseudo-second-order kinetic model exhibited higher R^2 values compared to the pseudo-first-order model (Fig. S6) for both low and high concentrations. Moreover, the q_e values obtained from the pseudo-second-order kinetic model fitting showed better agreement with experimental data, suggesting that the adsorption process of PS on UMF was controlled by chemical adsorption on the available binding sites of UMF [39,40]. We employed the intra-particle diffusion model (Fig. 4e and f) to gain deeper insights into the diffusion and adsorption behavior of PS. At low concentrations, the two linear segments in the model represented external diffusion (Stage I) and adsorption equilibrium (Stage II), respectively. The adsorption process at high concentrations is further divided into three stages. The diffusion rate constants followed the order $K_{i1} > K_{i2} > K_{i3}$, indicating a gradual decrease in adsorption efficiency as the process progresses. The first stage corresponded to the initial surface adsorption, where PS transferred from water to the UMF surface, exhibiting the highest adsorption rate. The second stage involved intra-particle diffusion, where the reduction of active adsorption sites on the UMF surface and the diffusion of PS into the internal structure increased resistance, resulting in a slower adsorption rate. This suggests that the diffusion of PS into the sponge interior is the rate-limiting step. The third stage reached adsorption equilibrium, where the concentration of PS in water decreased and the adsorption sites of UMF approached saturation, further reducing the diffusion rate until equilibrium was achieved.

3.3. Adsorption isotherm

To further understand the adsorption behavior of PS on UMF, we conducted adsorption isotherm studies. Fig. 5a shows that the adsorption capacity of UMF increased as the PS concentration increased from 25 mg/L to 250 mg/L, reflecting the abundance of adsorption sites. At an initial concentration of 250 mg/L, saturation adsorption was achieved with an adsorption capacity of 125.2 mg/g. When the initial concentration was 100 mg/L, both the removal efficiency and adsorption capacity were relatively high, reaching a favorable balance.

Additionally, the Langmuir and Freundlich (Eqs. (6) and (7)) models were employed to interpret the adsorption isotherm data.

$$\frac{C_e}{q_e} = \frac{1}{bq_m} + \frac{C_e}{q_m} \tag{6}$$

$$\ln q_e = \ln K_F + \frac{1}{n} \ln C_e \tag{7}$$

where C_e (mg/L) represents the equilibrium concentration of PS in the solution, q_e (mg/g) denotes the equilibrium adsorption capacity of UMF for PS, b (L/mg) is the Langmuir model adsorption constant, q_m (mg/g) signifies the maximum adsorption capacity, K_F [(mg/g)·(L/mg)$^{1/n}$] is

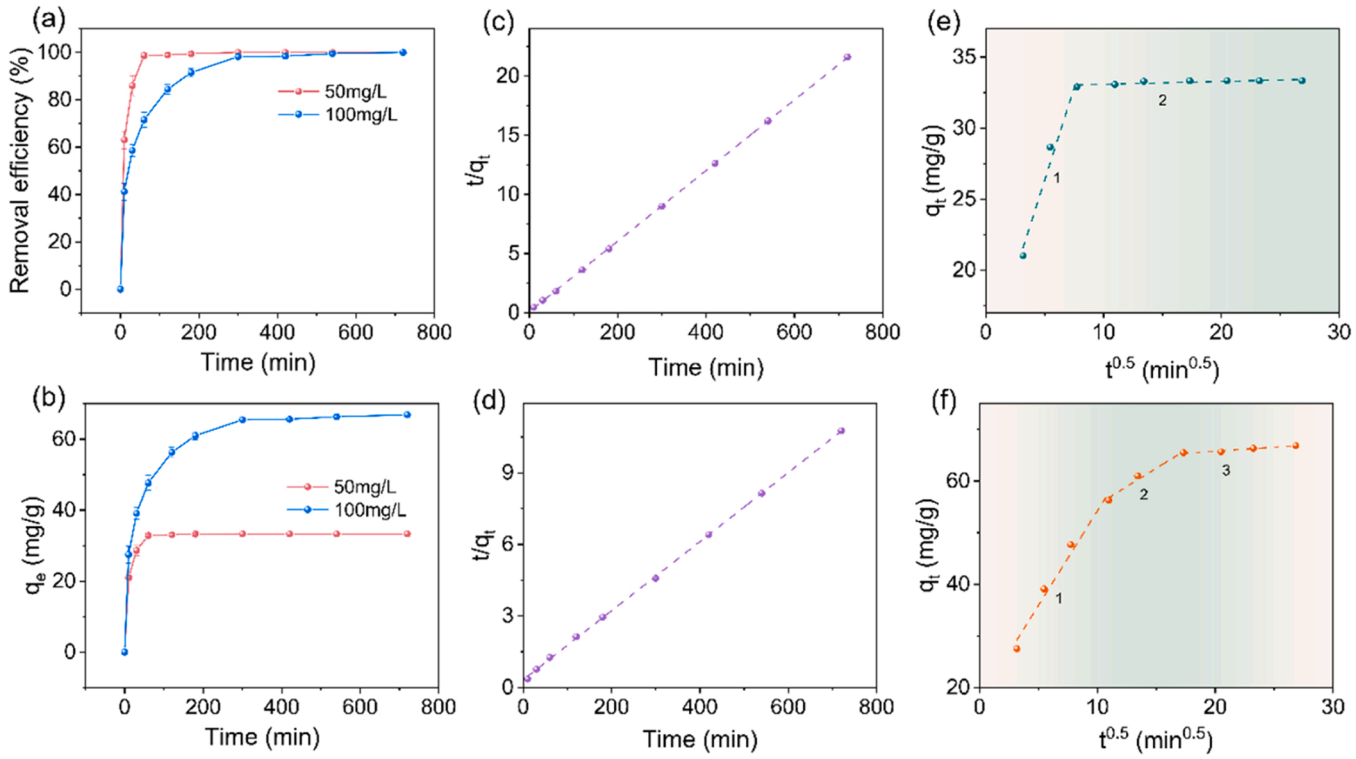

Fig. 4. (a)The removal efficiency and (b) the adsorption capacity of UMF for PS adsorption, (c), (d) the pseudo-second-order kinetic and (e), (f) the intra-particle diffusion model for 50 mg/L and 100 mg/L.

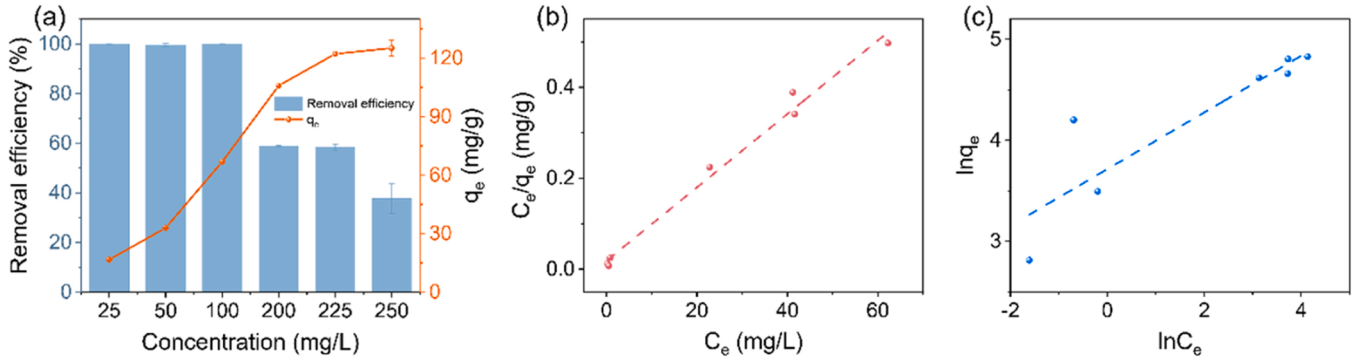

Fig. 5. (a) Removal efficiency and adsorption capacity of UMF for different concentrations of PS, (b) Langmuir model and (c) Freundlich model for PS adsorption by UMF.

the Freundlich model constant, and *n* indicate adsorption intensity.

Fig. 5b and c and Table S4 present the linear fitting results and parameter tables of the models. As indicated by the data in the table, compared to the Freundlich model ($R^2 = 0.8016$), the Langmuir model ($R^2 = 0.9255$) provided a better explanation of the adsorption behavior, with a simulated maximum adsorption capacity as high as 123.76 mg/g. According to the assumptions of the Langmuir model, the adsorption of PS on the UMF surface follows a monolayer adsorption mechanism [41]. Notably, the n value calculated from the Freundlich model is greater than 1, suggesting that the adsorption process is favorable and UMF is a suitable material for PS removal.

3.4. *Effect of pH*

pH is a crucial factor influencing the adsorption process as it directly affects the charge intensity on both PS and UMF surfaces, thereby further influence the adsorption performance [42]. Fig. 6a illustrates the removal efficiency of PS by UMF within the pH range of 3–10. In the pH ranges from 3 to 5, the removal efficiency of PS by UMF approached nearly 100 %. The removal efficiency of UMF had a declining trend with the increased pH value but kept at 93 % at pH 10. These results showed that the adsorption of PS by UMF was less affected by pH variations, likely attributable to weak electrostatic interactions. To better understand the influence of pH on PS removal by UMF, the zeta potentials of both UMF and PS were measured. Since the zeta potential of UMF could not be determined experimentally, we used UIO-66 as a surrogate to measure zeta potential under identical conditions. The zeta potential of UIO-66 powder was measured to represent the surface charge of the MOF component within the UMF composite. The isoelectric point of UIO-66 was approximately 5.0, suggesting that UMF carried a positive charge when the pH was below the isoelectric point and a negative charge when the pH was above it (Fig. 6b). PS consistently showed a negative surface charge across different pH values, with the negative zeta potential being more pronounced under alkaline conditions. Zeta

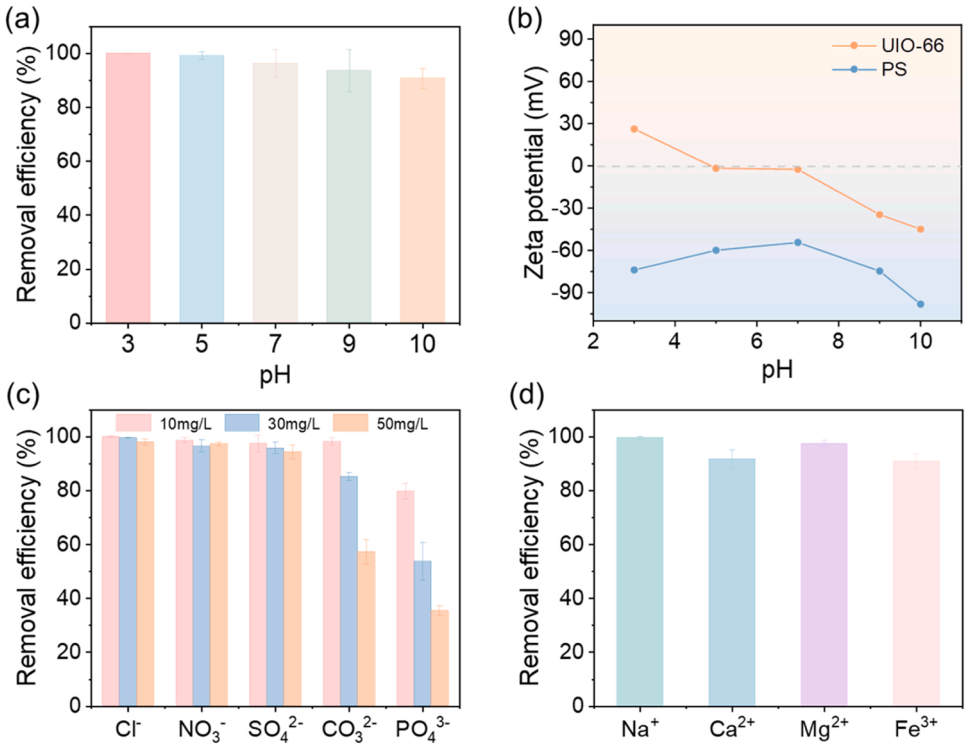

Fig. 6. (a) Effect of pH on PS adsorption by UMF, (b) Zeta potential of UIO-66 and PS at different pH, (c) Effect of anions and (d) cations (30 mg/L) on PS removal (UMF: 15 mg, PS: 100 mg/L, 300 min, 25 °C).

potential analysis revealed that at pH 3–5, the positive charge on UMF and the negative charge on PS induced electrostatic attraction, leading to excellent removal performance. Under alkaline conditions, since both UMF and PS carry negative charges, electrostatic repulsion occurred, and OH^- in the solution competed with negatively charged PS for adsorption sites on UMF [43], causing a slight decrease in PS adsorption efficiency. In addition, dynamic light scattering (DLS) analysis was used to evaluate the effect of pH (3−10) on the stability of PS NPs. It is noteworthy that the particle size distribution and stability of PS NPs remained largely unaffected within the tested pH range (Fig. S7). This behavior can be attributed to the stable negative surface charge of the PS, with zeta potentials ranging from approximately −54 to −91 mV. The resulting electrostatic repulsion between particles effectively maintained their dispersion in solution. This key finding indicates that pH does not serve as a primary factor governing the aggregation or dispersion of PS in the present system. Consequently, the influence of pH on the interaction between PS and UMF via changes in particle size or aggregation state was excluded. The high removal efficiency of UMF across a wide pH range in aqueous environments demonstrates the effectiveness of UMF in adsorbing PS.

3.5. Effect of interference ions

Generally, the presence of other cations and anions in aquatic environments can compete with PS for adsorption sites, thereby reducing PS removal efficiency. Therefore, the interference of typical anions and cations on PS adsorption in water was investigated. According to Fig. 6c, Cl^-, NO_3^-, and SO_4^{2-} had minimal impact on PS adsorption at both low and high concentrations. However, the removal efficiency of PS significantly decreased with increasing concentrations of CO_3^{2-} and PO_4^{3-}. The pH values of aqueous solutions with different concentrations of CO_3^{2-} and PO_4^{3-} are listed in Table S5. When CO_3^{2-} is present in aquatic environments, it readily converts to HCO_3^-, which increased pH value and weakened the electrostatic attraction between PS and the material [44, 45]. Additionally, CO_3^{2-} can be adsorbed onto UMF as a competing anion, occupying its adsorption sites. PO_4^{3-} exhibits similar effects as CO_3^{2-}, and due to its high charge density, the competitive effect was more pronounced [46]. As to the cations (Fig. 6d), the adsorption capacity of PS was significantly affected by Ca^{2+} and Fe^{3+}, while the presence of the other two cations Na^+ and Mg^{2+} showed no notable impact on removal efficiency. This is because Ca^{2+} adsorbs onto the material surface, and its large hydrated ionic radius forms a thick hydration layer, hindering contact between PS particles and active sites [47]. The strongly positively charged Fe^{3+} may bind with negatively charged PS via electrostatic interactions, resulting in partial retention of PS in the solution phase rather than adsorption onto UMF [48].

3.6. Adsorption mechanisms

The morphologies of the UMF adsorbent after PS adsorption were observed using SEM (Fig. S8). UMF maintained its porous structure after adsorption, with numerous PS particles visible on the UMF surface, suggesting the successful adsorption of PS by UMF and the stability of its structure. Fig. 7a presents the FTIR spectra of UMF before and after PS adsorption. After adsorption, new peaks appeared at 2924 and 2850 cm^{-1} in UMF-PS, representing the asymmetric and symmetric stretching vibrations of CH_2 in the vinyl group. The peak at 698 cm^{-1} corresponded to the out-of-plane bending vibration of the benzene ring in PS [49], further confirming successful PS adsorption. Additionally, since both UMF and PS contained benzene rings, and the C═C peak shifted after adsorption, the interaction of π-π stacking between PS and the benzene rings of UIO-66 contributed to the adsorption [50].

XPS analysis was also conducted to examine the chemical states of surface elements before and after PS adsorption, providing further insights into the adsorption mechanism. The XPS survey spectrum of UMF (Fig. 7b) shows peaks for C, N, O, and Zr, with high-resolution analysis performed on C 1 s, O 1 s, N 1 s and Zr 3d. For UMF, the C 1 s spectrum (Fig. 7c) exhibited peaks at 284.80, 285.83 and 288.92 eV, corresponding to C-C, C-O, and C═O, respectively [51]. The N 1 s spectrum (Fig. 7d) detected C═N and C-N from MF [52]. After adsorption, the

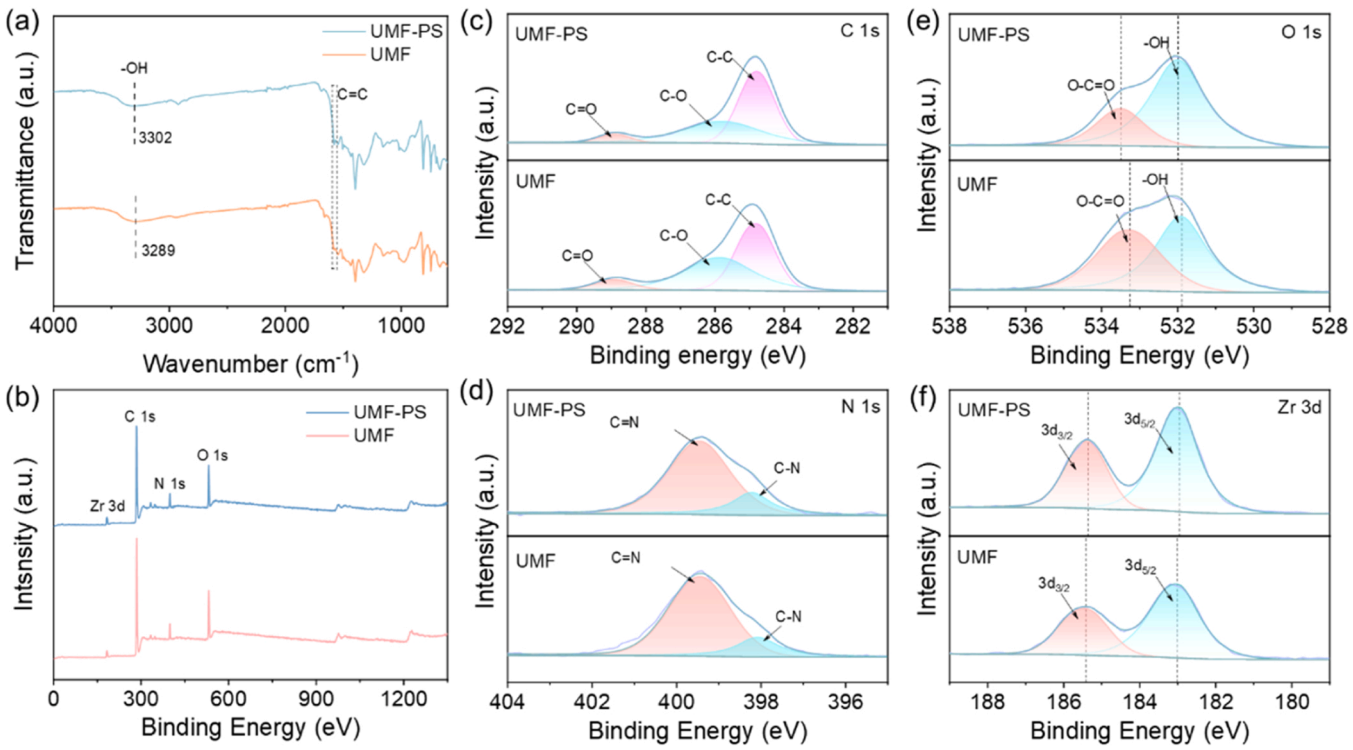

Fig. 7. (a) FTIR spectra of UMF before and after adsorption, (b) XPS full spectra of UMF and UMF-PS and the high resolution spectra of (c) C 1S, (d) O 1S, (e) N 1S, and (f) Zr 3d.

binding energies of -OH and O-C═O in the O 1 s spectrum increased [53] (Fig. 7e), which may be attributed to the formation of C═O-π and O-H-π interactions between the benzene rings of PS and the C═O/O-H groups in UMF [54,55]. These interactions, known as π-hydrogen bonds, may result in a loss of electron density of the C═O and O-H groups, leading to an increase in their binding energy [54]. The significant shift of the -OH peak in the FTIR spectrum further confirms the formation of hydrogen bonds. Additionally, the binding energy of Zr 3d decreased (Fig. 7f), suggesting that Zr may interact with the electron-rich benzene rings in PS through cation-π interactions [56]. The framework of UIO-66 is formed by $Zr_6O_4(OH)_4$ metal clusters (Zr_6 clusters) coordinated with H_2BDC ligands [57]. Some ligands might be lost in the synthesizing process, which produces open metal sites on the Zr_6 clusters. The Zr at these sites exhibits Lewis acidity (electron acceptor) and played as active center in the adsorption process [58]. Consequently, Zr readily accepts electrons from the benzene ring, thus its electron density increased and its binding energy decreased [59].

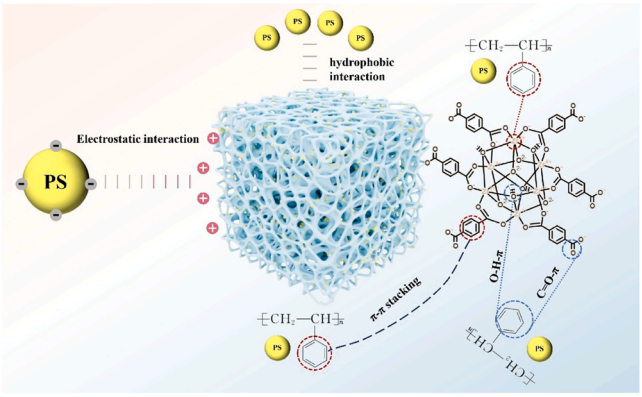

Fig. 8. Schematic diagram of the multiple driving forces for PS to adsorbed on UMF.

Combining SEM, FTIR, and XPS results, this study reveals that PS adsorbed onto UMF is a synergistically driven by multiple interactions (Fig. 8). The inherent three-dimensional macroporous structure of the UMF carrier facilitates PS diffusion and significantly enhances contact efficiency. Furthermore, multiple intermolecular interactions reinforce adsorption stability. Hydrophobic forces and electrostatic attraction draw PS particles closer to the UMF surface, creating favorable conditions for subsequent π-π stacking, π-hydrogen bonding and cation-π interactions. This synergy between physical and intermolecular forces enables UMF to efficiently and stably capture PS while effectively resisting competitive interference from other substances in aqueous environments. This provides a novel approach for designing highly effective adsorbents for MPs/NPs removal.

3.7. *Adsorption performance in actual aqueous environment*

To further evaluate the MPs removal potential of UMF in real-world environments, we applied UMF to three typical water systems, including tap water, river water and sea water. From Fig. 9a, UMF displayed near 100 % adsorption in both deionized water and sea water, while the adsorption efficiency decreased to 84.13 % and 82.53 % in tap water and river water, respectively. Few research on analyzing the reasons for the decreased adsorption efficiency in tap and river water could be found in references [11,20], so we conducted an in-depth investigation on how the factors affecting adsorption in these two types water. First, we measured the pH of the four kinds of water. The pH values of deionized water, tap water, river water and sea water were of 6.0, 7.6, 7.3 and 7.5, respectively. When we adjusted the pH of tap water (7.6) and river water (7.3) to 6.0, their adsorption efficiencies increased from 84.13 % and 82.53–91.34 % and 88.29 %, respectively (Fig. S9). This indicated that the electrostatic interaction between UMF and PS decreased with the elevated pH. While for the case of sea water, the bridging effect of Mg^{2+} might create new adsorption sites on the adsorbent surface [18]. Secondly, the total organic carbon (TOC) concentrations in tap water and river water were measured as 1.49 and

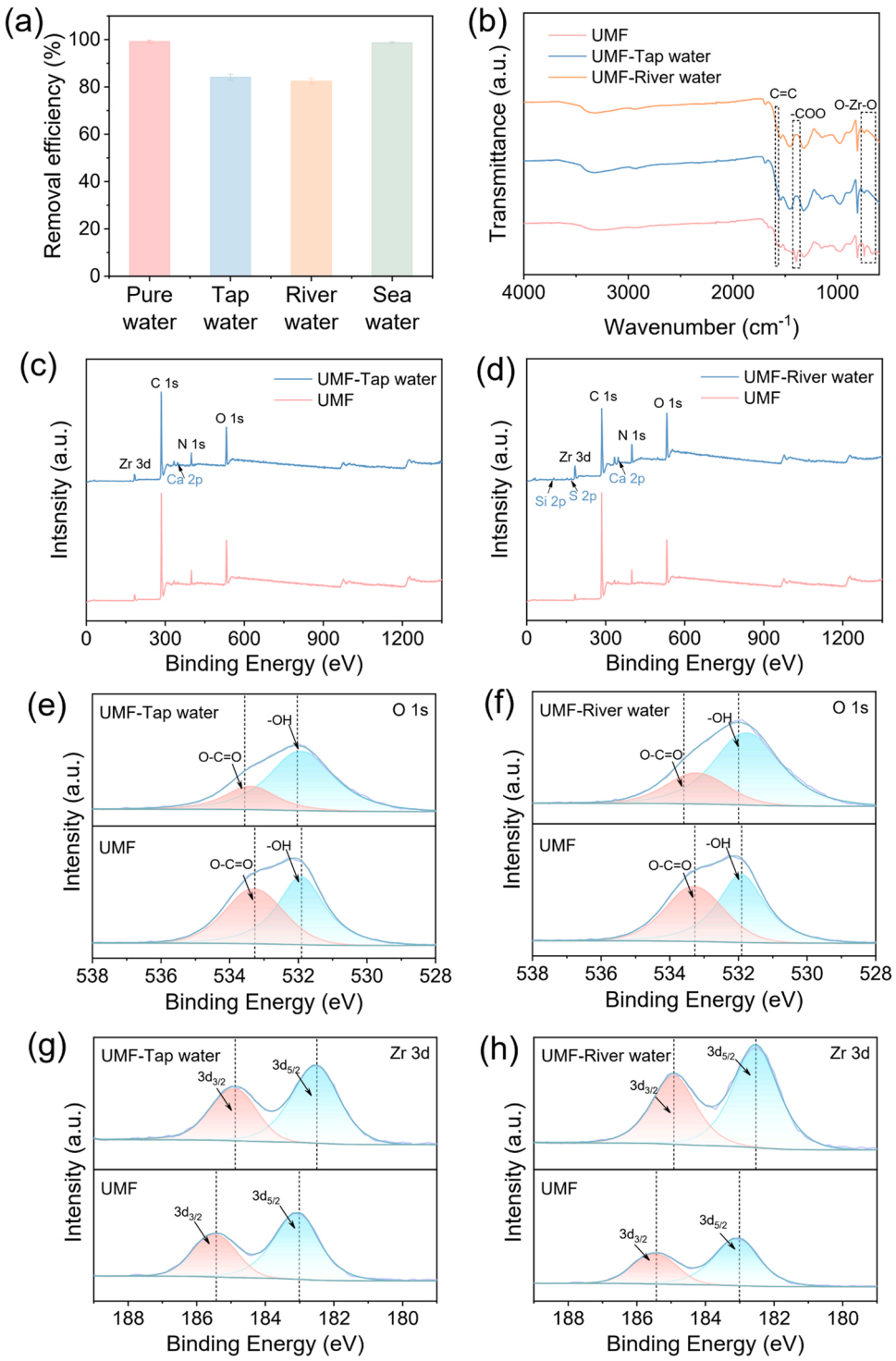

Fig. 9. (a) Removal efficiency of UMF for PS in real water, (b) FTIR spectra of UMF, UMF-Tap water and UMF-River water, XPS full spectra (c) and (d) and high resolution spectra of UMF-Tap water and UMF-River water (e), (f) O 1S and (g), (h) Zr 3d.

2.18 mg/L, respectively, both higher than that in sea water (1.23 mg/L). The elevated TOC levels might compete for adsorption sites on the material surface, thereby inhibiting the effective adsorption of PS and resulting in reduced removal efficiency. Additionally, we performed water quality analysis on tap water and river water, with results shown in Table S6. The analysis revealed that both tap water and river water contain significant amounts of Ca^{2+}, SO_4^{2-} and CO_3^{2-}, which might compete with PS for adsorption. This result also corresponds to the ion interference adsorption in the previous section (Section 3.5). FTIR and XPS analyses on UMF samples soaked in tap water and river water were conducted. The FTIR spectra (Fig. 9b) showed that the C═C and -COO peaks disappeared in UMF-Tap water and UMF-River water, and the Zr-O peak weakened. We attributed this to the formation of a deposition layer on the UMF surface from impurities (e.g., Ca^{2+}, SO_4^{2-} and sediment) in tap water and river water, which masked the FTIR signals of UIO-66. This hypothesis was supported by the XPS survey spectra (Fig. 9c and d), where Ca element was detected in tap water, and Ca, S, and Si (from sediment) were found in river water. High-resolution O 1 s

spectra (Fig. 9e and f) showed the increased binding energy for UMF-Tap water and UMF-River water, indicating ion adsorption onto the oxygenated ligands. The Zr 3d binding energy decreased (Fig. 9g and h), suggesting competitive ion adsorption onto the Zr clusters. In summary, UMF still achieved over 82 % adsorption efficiency in tap water and river water, demonstrating its potential for application in aqueous environments.

3.8. Cycling performance

Recycling performance is a critical indicator for evaluating the practical application of adsorbent materials in aqueous solution treatment. To assess the recycling performance of UMF for PS adsorption, we conducted 25 adsorption-desorption cycles on UMF samples. From Fig. 10a, after 18 cycles, the adsorption efficiency of PS slightly decreased to 91.76 %, and the efficiency remained at 81.39 % after 25 cycles. To elucidate the underlying mechanism responsible for the decreased removal efficiency, structural characterization of the recycled UMF was conducted. SEM analysis (Fig. S10a) revealed slight detachment of UIO-66 from the composite after repeated use. Concurrently, the FTIR spectra exhibited a marked reduction in the intensity of peaks (C═C, -COO and O-Zr-O) associated with active sites (Fig. 10b), and the specific surface area (33.22 m^2/g) showed a measurable decline (Fig. S10b). The above characterization results collectively indicated that the partial loss of UIO-66 is the main factor for the decreased adsorption. Considering the potential leaching of MOF components into aqueous medium, metal ion concentrations in solution after multiple cycles were quantified by ICP-MS (Table S7). The results showed Zr element content was 0.035 μg/L after 1st cycle and decreased to 0.011 μg/L after 25 cycles, both at extremely low levels. These results demonstrate that UMF exhibits excellent cycling stability and can serve as a potential adsorbent for treating MPs/NPs-polluted water.

We also conducted large-volume, low-concentration adsorption experiments to simulate natural MPs concentrations. Using UMF to adsorb 10 mg/L PS NPs (100 mL), the solution became clear after adsorption (Fig. S11), achieving 98 % adsorption efficiency.

We have conducted a comprehensive comparison of the removal performance of various adsorbents as shown in Table S8. Most current methods are either time-consuming, have low adsorption capacities, or both. Compared to these reported methods, our UMF demonstrates outstanding removal efficiency, high adsorption capacity, rapid adsorption and stable cycling performance.

3.9. Future development and cost analysis of UMF

Although UMF combines the high adsorption capacity of UIO-66 with the structural advantages of MF, the widespread use of the highly toxic solvent DMF in its synthesis process has limited its large-scale application. To overcome this obstacle, future efforts will focus on developing aqueous or green solvent synthesis routes to enhance its environmental friendliness and engineering feasibility. As to application prospects, UMF is suitable for pretreating industrial wastewater with concentrated MPs discharges, such as from laundries and cosmetics manufacturing plants. An assessment of the synthesis and operational expenses of UMF (Table S9) indicated a removal cost of only $2.61 per gram of PS, demonstrating significant economic advantages over other adsorbent materials. In summary, owing to its simple synthesis method and high cost-effectiveness, UMF holds potential for large-scale production and is expected to be applied in the efficient recovery and treatment of MPs/NPs.

4. Conclusion

In this study, we successfully prepared UMF composite with UIO-66 loaded on porous MF. The composite possesses a high specific surface area and excellent adsorption performance. The high specific surface area and abundant adsorption sites of UIO-66 endow the material with efficient adsorption capacity for MPs, while the flexibility and mechanical stability of MF ensure the reusability of the composite. UMF overcame the difficulty of solid-liquid separation of MOF powders and retained the low-density characteristics and simple operability. UMF achieved nearly 100 % adsorption efficiency for PS NPs, with an adsorption capacity of up to 65.5 mg/g. Additionally, UMF maintained a removal efficiency above 93 % across a wide pH range, enabling broad applicability in water with varying acidity and alkalinity. UMF remained an adsorption efficiency of over 82 % in actual aqueous environments such as tap water, river water, and sea water. Notably, UMF kept 81.39 % removal efficiency after 25 consecutive adsorption-desorption cycles, indicating strong cyclic stability with minimal loss of the active component (UIO-66). UMF adsorbed PS NPs through hydrophobic interactions, electrostatic interactions, π-π stacking, hydrogen bonds and cation-π interactions synergistically. Our research provides a strategy for efficient removal of MPs and NPs in various aqueous environments.

Environmental implication

This study develops a UMF composite by in-situ growth of UiO-66 on melamine foam (MF), which effectively resolves the critical issues of MOF powder aggregation and separation challenges. The composite demonstrates the efficient capture of nanoplastics, along with outstanding environmental stability and recyclability, providing a promising solution for nanoplastic pollution remediation in complex aquatic environments.

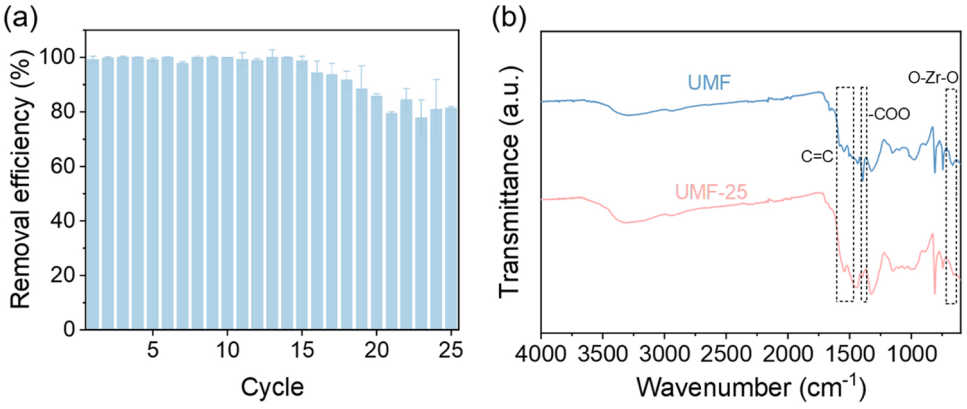

Fig. 10. (a) Cycling performance of PS removal by UMF with PS concentration of 50 mg/L, (b) FTIR spectrum after 25 cycles of UMF.

CRediT authorship contribution statement

Guanqing Song: Methodology. **Guanhong Lu:** Investigation. **Yan Wang:** Methodology, Investigation. **Jing Sun:** Writing – review & editing, Supervision, Project administration, Funding acquisition. **Shiqian Zhou:** Writing – review & editing, Writing – original draft, Validation, Methodology, Investigation. **Xiao Wang:** Methodology, Investigation. **Xujing Chen:** Methodology, Investigation. **Shijie Yang:** Methodology. **Kai Chen:** Methodology, Investigation.

Declaration of Competing Interest

The authors declare that they have no known competing financial interests or personal relationships that could have appeared to influence the work reported in this paper.

Acknowledgements

This work was financially supported by the funding from the State Key Lab of High Performance Ceramics and Superfine Microstructure.

Appendix A. Supporting information

Supplementary data associated with this article can be found in the online version at doi:10.1016/j.jhazmat.2025.140171.

Data availability

Data will be made available on request.

References

[1] Ye, S., Cheng, M., Zeng, G., Tan, X., Wu, H., Liang, J., et al., 2020. Insights into catalytic removal and separation of attached metals from natural-aged microplastics by magnetic biochar activating oxidation process. Water Res 179, 115876. https://doi.org/10.1016/j.watres.2020.115876.

[2] Wang, C., Zhao, J., Xing, B., 2021. Environmental source, fate, and toxicity of microplastics. J Hazard Mater 407, 124357. https://doi.org/10.1016/j.jhazmat.2020.124357.

[3] Wang, J., Zhao, X., Wu, F., Niu, L., Tang, Z., Liang, W., et al., 2021. Characterization, occurrence, environmental behaviors, and risks of nanoplastics in the aquatic environment: current status and future perspectives. Fundam Res 1 (3), 317–328. https://doi.org/10.1016/j.fmre.2021.05.001.

[4] Chen, Z., Shi, X., Zhang, J., Wu, L., Wei, W., Ni, B.-J., 2023. Nanoplastics are significantly different from microplastics in urban waters. Water Res X 19, 100169. https://doi.org/10.1016/j.wroa.2023.100169.

[5] Ragusa, A., Svelato, A., Santacroce, C., Catalano, P., Notarstefano, V., Carnevali, O., et al., 2021. Plasticenta: first evidence of microplastics in human placenta. Environ Int 146, 106274. https://doi.org/10.1016/j.envint.2020.106274.

[6] Galloway, T.S., Lewis, C.N., 2016. Marine microplastics spell big problems for future generations. Proc Natl Acad Sci 113 (9), 2331–2333. https://doi.org/10.1073/pnas.1600715113.

[7] Leslie, H.A., van Velzen, M.J.M., Brandsma, S.H., Vethaak, A.D., Garcia-Vallejo, J. J., Lamoree, M.H., 2022. Discovery and quantification of plastic particle pollution in human blood. Environ Int 163, 107199. https://doi.org/10.1016/j.envint.2022.107199.

[8] Pironti, C., Notarstefano, V., Ricciardi, M., Motta, O., Giorgini, E., Montano, L., 2023. First evidence of microplastics in human urine, a preliminary study of intake in the human body. Toxics 11 (1), 40. https://doi.org/10.3390/toxics11010040.

[9] Liu, S., Guo, J., Liu, X., Yang, R., Wang, H., Sun, Y., et al., 2023. Detection of various microplastics in placentas, meconium, infant feces, breastmilk and infant formula: a pilot prospective study. Sci Total Environ 854, 158699. https://doi.org/10.1016/j.scitotenv.2022.158699.

[10] Garcia, M.A., Liu, R., Nihart, A., El Hayek, E., Castillo, E., Barrozo, E.R., et al., 2024. Quantitation and identification of microplastics accumulation in human placental specimens using pyrolysis gas chromatography mass spectrometry. Toxicol Sci 199 (1), 81–88. https://doi.org/10.1093/toxsci/kfae021.

[11] Li, Y., Zhang, S., Liu, S., Chen, Y., Luo, M., Li, J., et al., 2024. Eco-friendly hydrophobic ZIF-8/sodium alginate monolithic adsorbent: an efficient trap for microplastics in the aqueous environment. J Colloid Interface Sci 661, 259–270. https://doi.org/10.1016/j.jcis.2024.01.182.

[12] Chen, R., Zhang, H., Lin, D., Wang, J., Guo, Y., Tang, X., et al., 2023. Potential negative effects of illumination on gravity-driven membrane system in treating sulfamethoxazole-containing water. Resour Conserv Recycl 190, 106839. https://doi.org/10.1016/j.resconrec.2022.106839.

[13] Hu, M., Palić, D., 2020. Micro- and nano-plastics activation of oxidative and inflammatory adverse outcome pathways. Redox Biol 37, 101620. https://doi.org/10.1016/j.redox.2020.101620.

[14] Zhou, Y., Ashokkumar, V., Amobonye, A., Bhattacharjee, G., Sirohi, R., Singh, V., et al., 2023. Current research trends on cosmetic microplastic pollution and its impacts on the ecosystem: a review. Environ Pollut 320, 121106. https://doi.org/10.1016/j.envpol.2023.121106.

[15] Li, L., Liu, D., Song, K., Zhou, Y., 2020. Performance evaluation of MBR in treating microplastics polyvinylchloride contaminated polluted surface water. Mar Pollut Bull 150, 110724. https://doi.org/10.1016/j.marpolbul.2019.110724.

[16] Zhang, Y., Diehl, A., Lewandowski, A., Gopalakrishnan, K., Baker, T., 2020. Removal efficiency of micro-and nanoplastics (180 nm-125 μm) during drinking water treatment. Sci Total Environ 720, 137383. https://doi.org/10.1016/j.scitotenv.2020.137383.

[17] Zhuang, J., Rong, N., Wang, X., Chen, C., Xu, Z., 2022. Adsorption of small size microplastics based on cellulose nanofiber aerogel modified by quaternary ammonium salt in water. Sep Purif Technol 293, 121133. https://doi.org/10.1016/j.seppur.2022.121133.

[18] Ramirez Arenas, L., Ramseier Gentile, S., Zimmermann, S., Stoll, S., 2021. Nanoplastics adsorption and removal efficiency by granular activated carbon used in drinking water treatment process. Sci Total Environ 791, 148175. https://doi.org/10.1016/j.scitotenv.2021.148175.

[19] Singh, N., Khandelwal, N., Ganie, Z.A., Tiwari, E., Darbha, G.K., 2021. Eco-friendly magnetic biochar: an effective trap for nanoplastics of varying surface functionality and size in the aqueous environment. Chem Eng J 418, 129405. https://doi.org/10.1016/j.cej.2021.129405.

[20] Fu, J., Liu, N., Peng, Y., Wang, G., Wang, X., Wang, Q., et al., 2023. An ultra-light sustainable sponge for elimination of microplastics and nanoplastics. J Hazard Mater 456, 131685. https://doi.org/10.1016/j.jhazmat.2023.131685.

[21] Sun, C., Wang, Z., Chen, L., Li, F., 2020. Fabrication of robust and compressive chitin and graphene oxide sponges for removal of microplastics with different functional groups. Chem Eng J 393, 124796. https://doi.org/10.1016/j.cej.2020.124796.

[22] Zhang, Y., Yuan, S., Feng, X., Li, H., Zhou, J., Wang, B., 2016. Preparation of nanofibrous metal-organic framework filters for efficient air pollution control. J Am Chem Soc 138 (18), 5785–5788. https://doi.org/10.1021/jacs.6b02553.

[23] Kobielska, P.A., Howarth, A.J., Farha, O.K., Nayak, S., 2018. Metal-organic frameworks for heavy metal removal from water. Coord Chem Rev 358, 92–107. https://doi.org/10.1016/j.ccr.2017.12.010.

[24] Rego, R.M., Ajeya, K.V., Jung, H.-Y., Kabiri, S., Jafarian, M., Kurkuri, M.D., et al., 2023. Nanoarchitectonics of bimetallic MOF@Lab-Grade flexible filter papers: an approach towards Real-Time water decontamination and circular economy. Small 19 (45), 2302692. https://doi.org/10.1002/smll.202302692.

[25] Mane, P.V., Rego, R.M., Yap, P.L., Losic, D., Kurkuri, M.D., 2024. Unveiling cutting-edge advances in high surface area porous materials for the efficient removal of toxic metal ions from water. Prog Mater Sci 146, 101314. https://doi.org/10.1016/j.pmatsci.2024.101314.

[26] Wan, H., Wang, J., Sheng, X., Yan, J., Zhang, W., Xu, Y., 2022. Removal of polystyrene microplastics from aqueous solution using the Metal-Organic framework material of ZIF-67. Toxics 10 (2), 70. https://doi.org/10.3390/toxics10020070.

[27] Modak, S., Kasula, M., Esfahani, M.R., 2023. Nanoplastics removal from water using Metal-Organic framework: investigation of adsorption mechanisms, kinetics, and effective environmental parameters. ACS Appl Eng Mater 1 (2), 744–755. https://doi.org/10.1021/acsaenm.2c00174.

[28] Mo, Z., Tai, D., Zhang, H., Shahab, A., 2022. A comprehensive review on the adsorption of heavy metals by zeolite imidazole framework (ZIF-8) based nanocomposite in water. Chem Eng J 443, 136320. https://doi.org/10.1016/j.cej.2022.136320.

[29] Siddiqui, S.A., Singh, S., Bahmid, N.A., Shyu, D.J.H., Domínguez, R., Lorenzo, J.M., et al., 2023. Polystyrene microplastic particles in the food chain: characteristics and toxicity - a review. Sci Total Environ 892, 164531. https://doi.org/10.1016/j.scitotenv.2023.164531.

[30] Yu, J., Wang, X., Wang, Y., Xie, X., Xie, H., Vorayos, N., et al., 2024. Heating-induced adsorption promoting the efficient removal of toluene by the metal-organic framework UIO-66 (Zr) under visible light. J Colloid Interface Sci 653, 1478–1487. https://doi.org/10.1016/j.jcis.2023.09.164.

[31] Guan, H., Li, R., Lian, R., Cui, J., Ou, M., Liu, L., et al., 2023. A biomimetic design for efficient petrochemical spill disposal: CoFe-PBA modified superhydrophobic melamine sponge with mechanical/chemical durability and low fire risk. J Hazard Mater 459, 132041. https://doi.org/10.1016/j.jhazmat.2023.132041.

[32] Xu, W., Dong, M., Di, L., Zhang, X., 2019. A facile method for preparing UIO-66 encapsulated ru catalyst and its application in Plasma-Assisted CO_2 methanation. Nanomaterials 9 (10), 1432. https://doi.org/10.3390/nano9101432.

[33] Abid, H.R., Tian, H., Ang, H.-M., Tade, M.O., Buckley, C.E., Wang, S., 2012. Nanosize Zr-metal organic framework (UIO-66) for hydrogen and carbon dioxide storage. Chem Eng J 187, 415–420. https://doi.org/10.1016/j.cej.2012.01.104.

[34] Cui, Y., Sun, J., 2025. High-efficiency CO_2-epoxide cycloaddition using multifunctional ionic liquids grafted onto UIO-66-NH_2 under solvent /cocatalyst both-free conditions. Sep Purif Technol 358, 130269. https://doi.org/10.1016/j.seppur.2024.130269.

[35] Rodrigues, M.A., Ribeiro, Jd.S., Costa, Ed.S., Miranda, J.Ld, Ferraz, H.C., 2018. Nanostructured membranes containing UIO-66 (Zr) and MIL-101 (Cr) for O_2/N_2 and CO_2/N_2 separation. Sep Purif Technol 192, 491–500. https://doi.org/10.1016/j.seppur.2017.10.024.

[36] Valenzano, L., Civalleri, B., Chavan, S., Bordiga, S., Nilsen, M.H., Jakobsen, S., et al., 2011. Disclosing the complex structure of UIO-66 metal organic framework: a synergic combination of experiment and theory. Chem Mater 23 (7), 1700–1718. https://doi.org/10.1021/cm1022882.
[37] Liu, M., Liu, X., Zheng, S., Jia, K., Yu, L., Xin, J., et al., 2023. Environment-Friendly superhydrophobic sponge for highly efficient Oil/Water separation and microplastic removal. Sep Purif Technol 319, 124060. https://doi.org/10.1016/j.seppur.2023.124060.
[38] Mohan, B., Singh, K., Gupta, R.K., Kumar, A., Pombeiro, A.J.L., Ren, P., 2024. Water purification advances with metal-organic framework-based materials for micro/nanoplastic removal. Sep Purif Technol 343, 126987. https://doi.org/10.1016/j.seppur.2024.126987.
[39] Yao, W., Yu, S., Wang, J., Zou, Y., Lu, S., Ai, Y., et al., 2017. Enhanced removal of methyl Orange on calcined glycerol-modified nanocrystallined Mg/Al layered double hydroxides. Chem Eng J 307, 476–486. https://doi.org/10.1016/j.cej.2016.08.117.
[40] Chen, R., Cheng, Y., Wang, P., Wang, Y., Wang, Q., Yang, Z., et al., 2021. Facile synthesis of a sandwiched Ti3C2Tx MXene/nZVI/fungal hypha nanofiber hybrid membrane for enhanced removal of Be(II) from $Be(NH_2)_2$ complexing solutions. Chem Eng J 421, 129682. https://doi.org/10.1016/j.cej.2021.129682.
[41] Zhu, W., Lei, J., Li, Y., Dai, L., Chen, T., Bai, X., et al., 2019. Procedural growth of fungal hyphae/Fe_3O_4/graphene oxide as ordered-structure composites for water purification. Chem Eng J 355, 777–783. https://doi.org/10.1016/j.cej.2018.08.215.
[42] Xu, Y., Chen, J., Chen, R., Yu, P., Guo, S., Wang, X., 2019. Adsorption and reduction of chromium(VI) from aqueous solution using polypyrrole/calcium rectorite composite adsorbent. Water Res 160, 148–157. https://doi.org/10.1016/j.watres.2019.05.055.
[43] Liu, F.-f, Zhao, J., Wang, S., Du, P., Xing, B., 2014. Effects of solution chemistry on adsorption of selected pharmaceuticals and personal care products (PPCPs) by graphenes and carbon nanotubes. Environ Sci Technol 48 (22), 13197–13206. https://doi.org/10.1021/es5034684.
[44] Ganie, Z.A., Khandelwal, N., Tiwari, E., Singh, N., Darbha, G.K., 2021. Biochar-facilitated remediation of nanoplastic contaminated water: effect of pyrolysis temperature induced surface modifications. J Hazard Mater 417, 126096. https://doi.org/10.1016/j.jhazmat.2021.126096.
[45] Zhou, G., Huang, X., Xu, H., Wang, Q., Wang, M., Wang, Y., et al., 2022. Removal of polystyrene nanoplastics from water by CuNi carbon material: the role of adsorption. Sci Total Environ 820, 153190. https://doi.org/10.1016/j.scitotenv.2022.153190.
[46] Zhao, H., Huang, X., Wang, L., Zhao, X., Yan, F., Yang, Y., et al., 2022. Removal of polystyrene nanoplastics from aqueous solutions using a novel magnetic material: adsorbability, mechanism, and reusability. Chem Eng J 430, 133122. https://doi.org/10.1016/j.cej.2021.133122.
[47] Yang, J., Hou, D., Ding, Q., 2018. Ionic hydration structure, dynamics and adsorption mechanism of sulfate and sodium ions in the surface of calcium silicate hydrate gel: a molecular dynamics study. Appl Surf Sci 448, 559–570. https://doi.org/10.1016/j.apsusc.2018.04.071.
[48] Zhang, Y., Luo, Y., Guo, X., Xia, T., Wang, T., Jia, H., et al., 2020. Charge mediated interaction of polystyrene nanoplastic (PSNP) with minerals in aqueous phase. Water Res 178, 115861. https://doi.org/10.1016/j.watres.2020.115861.
[49] Olmos, D., Martín, E.V., González-Benito, J., 2014. New molecular-scale information on polystyrene dynamics in PS and PS-$BaTiO_3$ composites from FTIR spectroscopy. Phys Chem Chem Phys 16 (44), 24339–24349. https://doi.org/10.1039/C4CP03516J.
[50] Zhao, H., Jianhua, W., Fengmei, S., He, X., 2023. Removal of polystyrene nanoplastics from aqueous solutions by a novel magnetic zeolite adsorbent. Hum Ecol Risk Assess Int J 29 (2), 327–346. https://doi.org/10.1080/10807039.2022.2071209.
[51] Liu, Q., Ye, J., Han, Y., Wang, P., Fei, Z., Chen, X., et al., 2021. Defective UIO-67 for enhanced adsorption of dimethyl phthalate and phthalic acid. J Mol Liq 321, 114477. https://doi.org/10.1016/j.molliq.2020.114477.
[52] Zhu, X., Zhou, G., He, G., Ma, L., Xu, B., Sun, F., 2023. Directly loading graphene oxide into melamine sponge for fast and high-efficiency adsorption of methylene blue. Surf Interfaces 36, 102575. https://doi.org/10.1016/j.surfin.2022.102575.
[53] Li, M., Liu, Y., Li, F., Shen, C., Kaneti, Y.V., Yamauchi, Y., et al., 2021. Defect-Rich hierarchical porous UIO-66(Zr) for tunable phosphate removal. Environ Sci Technol 55 (19), 13209–13218. https://doi.org/10.1021/acs.est.1c01723.
[54] Wu, Y., Ye, C., Liu, F., Gu, X., Yu, L., Shi, X., et al., 2024. Highly efficient, recyclable microplastic adsorption enabled by chitin hydrogen bond network rearrangement. Adv Funct Mater 34 (32), 2311075. https://doi.org/10.1002/adfm.202311075.
[55] Di Mino, C., Seel, A.G., Clancy, A.J., Headen, T.F., Földes, T., Rosta, E., et al., 2023. Strong structuring arising from weak cooperative O-H···π and C-H···O hydrogen bonding in benzene-methanol solution. Nat Commun 14 (1), 5900. https://doi.org/10.1038/s41467-023-41451-y.
[56] Zhao, G., Zhu, H., 2020. Cation-π interactions in Graphene-Containing systems for water treatment and beyond. Adv Mater 32 (22), 1905756. https://doi.org/10.1002/adma.201905756.
[57] Trickett, C.A., Gagnon, K.J., Lee, S., Gándara, F., Bürgi, H.-B., Yaghi, O.M., 2015. Definitive molecular level characterization of defects in UIO-66 crystals. Angew Chem Int Ed 54 (38), 11162–11167. https://doi.org/10.1002/anie.201505461.
[58] Yu, J., Wang, X., Lu, G., Xie, H., Xie, X., Sun, J., 2024. Improving the removal efficiency of oxygenated volatile organic compounds by defective UIO-66 regulated with water. J Hazard Mater 469, 134055. https://doi.org/10.1016/j.jhazmat.2024.134055.
[59] Cao, Y., Chen, X., Li, X., Wang, B., 2021. Tuning surface functionalization and pore structure of UIO-66 Metal–Organic framework nanoparticles for organic pollutant elimination. ACS Appl Nano Mater 4 (5), 5486–5495. https://doi.org/10.1021/acsanm.1c00796.